



Engineering ordered vacancies and atomic arrangement over the intermetallic PdM/CNT (M = Pb, Sn, In) nanocatalysts for synergistically promoting electrocatalysis N₂ fixation

Zuochao Wang ^a, Jiao Liu ^a, Xueke Wu ^a, Nanzhu Nie ^{a,b}, Dan Zhang ^{a,b}, Hongdong Li ^a, Huan Zhao ^a, Jianping Lai ^{a, **}, Lei Wang ^{a,b,*}

^a Key Laboratory of Eco-chemical Engineering, Ministry of Education, International Science and Technology Cooperation Base of Eco-chemical Engineering and Green Manufacturing, College of Chemistry and Molecular Engineering, Qingdao University of Science and Technology, Qingdao 266042, PR China

^b Shandong Engineering Research Center for Marine Environment Corrosion and Safety Protection, College of Environment and Safety Engineering, Qingdao University of Science and Technology, Qingdao 266042, PR China



ARTICLE INFO

Keywords:
Ultrafast
Intermetallic
Ordered vacancies
Method
Electrocatalysis

ABSTRACT

The synthesis of intermetallic compounds with small size and defective structures is rigorous challenge. In this work, the small size (< 10 nm) of intermetallic PdM (M = Pb, Sn, In) with ordered vacancies (OVs) are successfully prepared by ultrafast and solvent-free microwave method for the first time. With the optimized vacancies, atomic arrangement and components, the intermetallic OVs-Pd₃Pb-2 shows the best nitrogen reduction (NRR) performance among intermetallic OVs-PdM (M = Sn, In), intermetallic OVs-Pd₃Pb with various degrees of vacancies, intermetallic Pd₃Pb with vacancies-free, Pd₃Pb/CNT and Pd/CNT in Li₂SO₄ solution. In situ Raman spectroscopy, *in situ* attenuated total reflectance surface-enhanced infrared absorption spectroscopy (ATR-SEIRAS) technique and density functional theory (DFT) further demonstrate the synergy mechanism of good NRR activity at low overpotentials on OVs-Pd₃Pb-2 catalysts.

1. Introduction

Ammonia (NH₃) is the most vital precursor for many agriculture, industry and medicine, and it is a key factor in determining social progress [1–4]. However, the industrial NH₃ synthesis method which mainly relies on Haber-Bosch (HB) process usually needs harsh environmental conditions such as high temperature and high pressure, which causes great harm to the environment [5–7]. As a green and sustainable route for NH₃ synthesis, electrocatalytic nitrogen reduction (NRR) is suitable for distributed and small batch production of NH₃ [8–10], which avoids secondary energy consumption in transportation and storage [11–14]. However, its low reactivity, stability and selectivity limit its wide application [15–18]. Therefore, the controllable synthesis of NRR electrocatalysts with high activity, high selectivity and high stability is of great significance [14,19–23].

Studies have shown that Pd-based nanomaterials have good NRR

activity at low overpotentials due to electrochemical formation of α -palladium hydride result in decreasing the free energy barrier of N₂ hydrogenation to *N_2H [24], the rate-limiting step for NH₃ production [25–28]. The ordered arrangement of atoms in the Pd-based intermetallic compound could promote can absorb N₂ molecules and lower the energy barrier of *N_2 for N₂ adsorption and activation to enhanced activity [29–32]. Furthermore, effective stabilization of $^*N_2/^*N_2H$ by introducing defects in Pd-based nanomaterials to break the proportionality while destabilizing $^*NH_2/^*NH_3$, resulting in lower energy barriers for more optimal binding affinity of NRR intermediates and enhanced material activity towards NRR [33–35]. Nevertheless, the development of such intermetallic catalysts with vacancies is still in its infancy, the synergistic effect of vacancies and intermetallic for the NRR demands more in-depth discussion.

The traditional synthesis method of intermetallic nanocrystals mainly include hydrothermal method and annealed method [36–38].

* Corresponding author at: Key Laboratory of Eco-chemical Engineering, Ministry of Education, International Science and Technology Cooperation Base of Eco-chemical Engineering and Green Manufacturing, College of Chemistry and Molecular Engineering, Qingdao University of Science and Technology, Qingdao 266042, PR China.

** Corresponding author.

E-mail addresses: jplai@qust.edu.cn (J. Lai), inorchemwl@126.com (L. Wang).

Most of them need long periods of time at high temperature to boost atomic migration and ordering [39–41], which not only unfavorable for large scale production due to long time operation [42], but also the synthesized ordered structure partially becomes disordered due to time-consuming high-temperature tends to thermodynamically stable state [43]. Furthermore, the nanocrystals aggregate and sinter at the conditions of long-time high-temperature, resulting in larger sizes (>10 nm) with wider size dispersion [38], and less susceptibility to defect formation thanks to the thermodynamically favorable steady, so that reduced exposure of active sites [44,45]. Therefore, the synthesis of intermetallic compounds with small size and defective structures is also a challenge.

In this work, the small size (<10 nm) of intermetallic PdM ($M = \text{Pb, Sn, In}$) with ordered vacancies (OVs) are successfully prepared by ultrafast and solvent-free microwave method for the first time. The microwave method is simple, rapid (60 s) and high production (82.0%), and the degree of defects can be adjusted by changing the microwave time. The synthesis of intermetallic compound catalysts can obtain gram-level products. With the optimized vacancies, atomic arrangement and components, the intermetallic OVs-Pd₃Pb-2 shows an outstanding nitrogen reduction (NRR) performance among intermetallic OVs-PdM ($M = \text{Sn, In}$), intermetallic OVs-Pd₃Pb with various degrees of vacancies, intermetallic Pd₃Pb with vacancies-free, Pd₃Pb alloy and Pd/CNT in Li₂SO₄ solution. In addition, the turnover frequency (TOF) of intermetallic OVs-Pd₃Pb-2 is better than Pd₃Pb without vacancies, indicating that intermetallic OVs-Pd₃Pb-2 catalyst has predominant intrinsic activity. In addition, *in situ* Raman spectroscopy, *in situ* attenuated total reflectance surface-enhanced infrared absorption spectroscopy (ATR-SEIRAS) technique and density functional theory (DFT) results further illustrate the synergy mechanism that the intermetallic OVs-Pd₃Pb-2 with the optimal defects has an outstanding NRR performance.

2. Methods and experimental section

2.1. Chemicals

Palladium acetylacetone (Pd(acac)₂, 99%), So-dium tetrachloropalladateand (Na₂PdCl₄, 98%) and Lead acetylacetone (Pb(acac)₂, 95%) were taken from Macklin. Citric acid (CA), and ethylene glycol (EG) were all bought from Sigma-Aldrich. Polyvinylpyrrolidone (PVP, MW= 55 000) was made from Aldrich. Tin tetrachloride (SnCl₄, 99.99%) and Indium chlo-ride (InCl₃, 98%) was gained from Aladdin. MWCNT was obtained from Aladdin.

2.2. Preparation of Pd/CNT

5 mg of MWCNT and 5 mg of Pd(acac)₂ were commingled and milled in a mortar for 30 min to make a homogeneous mixture. Then, the mixture was placed in a quartz vial and microwaved in a domestic microwave oven for 60 s to gain the Pd/CNT.

2.3. Preparation of intermetallic OVs-PdM ($M = \text{Pb, Sn, In}$)

First, 12 mg of MWCNT, 5 mg of Pd(acac)₂, and 6.7 mg of Pb(acac)₂ were commingled and milled in a mortar for 30 min to make a homogeneous mixture. Then, the mixture was placed in a quartz vial and microwaved in a domestic microwave oven for 60 s to gain the intermetallic OVs-Pd₃Pb/CNT (note as OVs-Pd₃Pb-2). The OVs-Pd₂Sn and OVs-Pd₃In were prepared by re-placing the Pb(acac)₂ with SnCl₄ (5.7 mg) and InCl₃ (3.6 mg) under the same conditions, respectively.

2.4. Preparation of intermetallic OVs-Pd₃Pb-X ($X = 1, 3, 4$)

First, 12 mg of MWCNT, 5 mg of Pd(acac)₂, and 6.7 mg of Pb(acac)₂ were commingled and milled in a mortar for 30 min to make a

homogeneous mixture. Then, the mixture was placed in a quartz vial and microwaved in a domestic microwave oven for 30 s to gain the OVs-Pd₃Pb/CNT (note as OVs-Pd₃Pb-1). The OVs-Pd₃Pb-x were prepared by changing various times in 120, and 180 s (note as OVs-Pd₃Pb-3 and OVs-Pd₃Pb-4) under the same conditions.

2.5. Preparation of intermetallic VFs-Pd₃Pb

First, 12 mg of MWCNT, 5 mg of Pd(acac)₂, and 6.7 mg of Pb(acac)₂ were commingled and milled in a mortar for 30 min to make a homogeneous mixture. Then, the mixture was placed in a quartz vial and microwaved in a domestic microwave oven for 15 s to gain the VFs-Pd₃Pb.

2.6. Preparation of Pd₃Pb alloy

7.1 mg of Na₂PdCl₄, 16.2 mg of Pb(acac)₂, 100 mg PVP, 10 mg CNT, and 48 mg of CA were mixed with 10 mL of EG, and then placed into a vial bottle to sonicated for 1 h until became the clear solution. The reaction at 170 °C for 1 h and after cooled down, it was washed with ethanol and water for three times.

3. Results and discussion

3.1. Catalysts synthesis and physical characterizations

The intermetallic OVs-PdM ($M = \text{Pb, Sn, In}$) catalysts were prepared by using multi-walled carbon nanotubes (MWCNT) (Figs. S1, 2) as a carrier in a household microwave oven for 60 s (Fig. S3). Under the impact of fast heating and cooling in a microwave oven, Pd with a small size (7.0 nm) is successfully loaded on MWCNT (Fig. S4, 5), which the whole process is simple, convenient and without adding any solvent. Otherwise, the Pd₃Pb were gained by one-pot way, which need the reducing agent (EG) and the surfactant (PVP) (for experimental details, please see the Methods). From Fig. S6a, it is clearly shown that the Pd₃Pb nanoparticles load on the MWCNT, and the X-ray diffraction (XRD) pattern (Fig. S6b) shows that peak positions were negatively shifted from those of the standard PDF card of Pd. The XRD of the intermetallic OVs-Pd₃Pb-2 catalyst matched nicely with the intermetallic Pd₃Pb reference (PDF#50–1631) as shown in Fig. 1a. Scanning electron microscope (SEM) and transmission electron microscope (TEM) were used to characterize the morphology of the intermetallic OVs-Pd₃Pb-2 catalyst. It is obviously shown in Fig. 1b–c, Fig. S7 and S8a, the nanoparticles were uniformly immobilized on CNT with an average size of about 7.3 nm. The high-resolution TEM (HRTEM, Fig. 1d) image displays that atomic lattice stripes of the intermetallic OVs-Pd₃Pb-2 catalyst and the lattice spacing is 0.23 nm, which can be considered as the (111) face of the intermetallic Pd₃Pb. The fast Fourier transform (FFT) (Fig. 1e) of the HRTEM pattern showed the visible Pb vacancies in the whole area. In addition, the TEM energy-dispersive X-ray spectroscopy (TEM-EDX) element mapping images (Fig. 1f) demonstrated that Pd and Pb elements are uniformly scattered on the nanoparticles. From the inductively coupled plasma atomic emission spectrometer (ICP-AES) analysis and XPS analysis (Tables S2–3), the surface molar ratios of Pd/Pb are changed by different microwave times, indicates that a number of Pb vacancies were formed. In addition, it is demonstrated from Fig. S9 that the synthesis of intermetallic OVs-Pd₃Pb-2 catalyst is mass-produced, which the raw materials are enlarged by 100 times, and experiments are performed to gain about 1.9433 g of product (the yield is 82.0%).

In order to study the effect of surface vacancies on the electronic structure of the catalysts, therefore different levels of vacancies were discussed. And the different extent of vacancies can be controlled by changing the various microwave times. As can be known from Fig. 2a, the XRD patterns of the as-prepared intermetallic VFs-Pd₃Pb and the intermetallic OVs-Pd₃Pb-X ($X = 1, 2, 3, 4$) with various degrees of vacancies catalysts show the same diffraction peaks, which confirm that

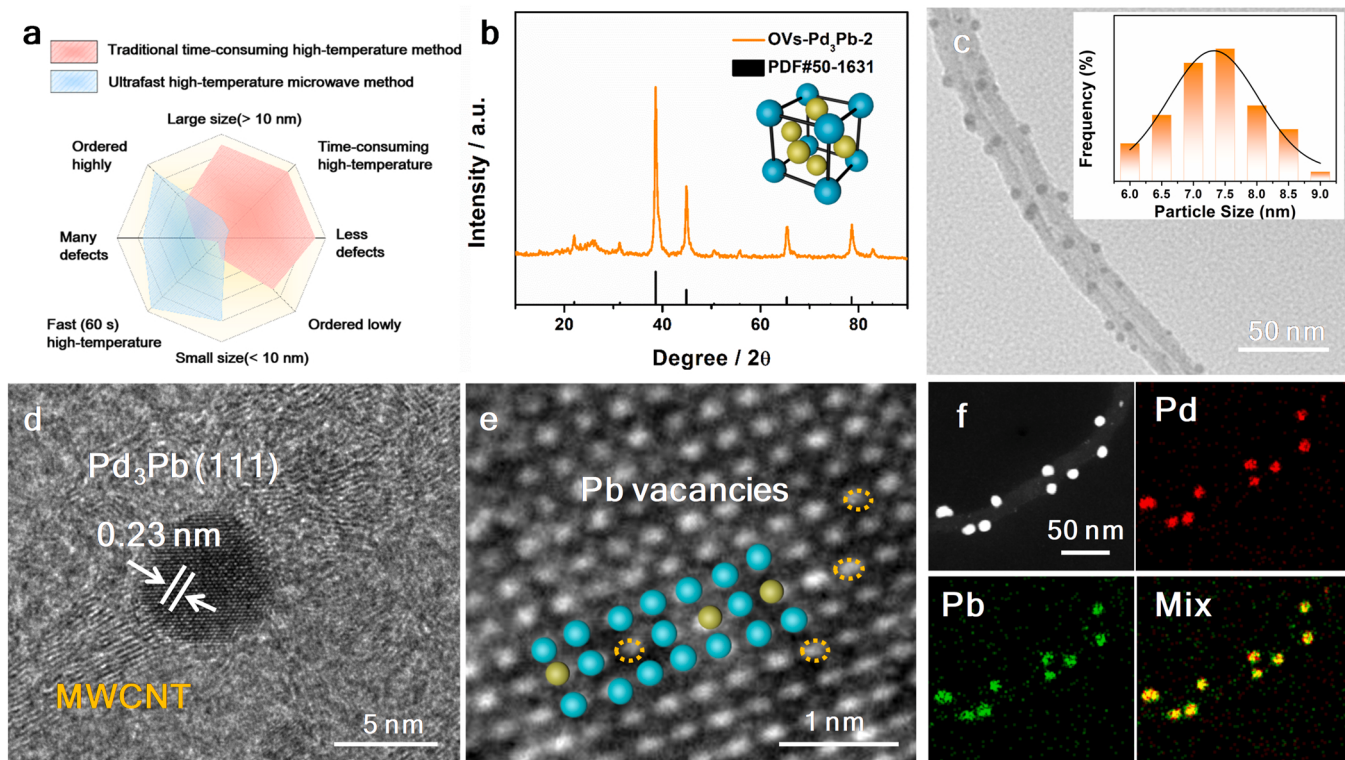


Fig. 1. (a) Comparison of advantages and disadvantages of ordered intermetallic synthesis methods. (b) The X-ray diffraction (XRD) pattern of OVs-Pd₃Pb-2. (c) TEM images of intermetallic OVs-Pd₃Pb-2, the inset (in c) is the particle size histogram of nanocrystals. (d, e) HRTEM images and FFT pattern of intermetallic OVs-Pd₃Pb-2, the yellow circles display Pb vacancies. (f) HAADF-STEM image and corresponding elemental mapping of intermetallic OVs-Pd₃Pb-2.

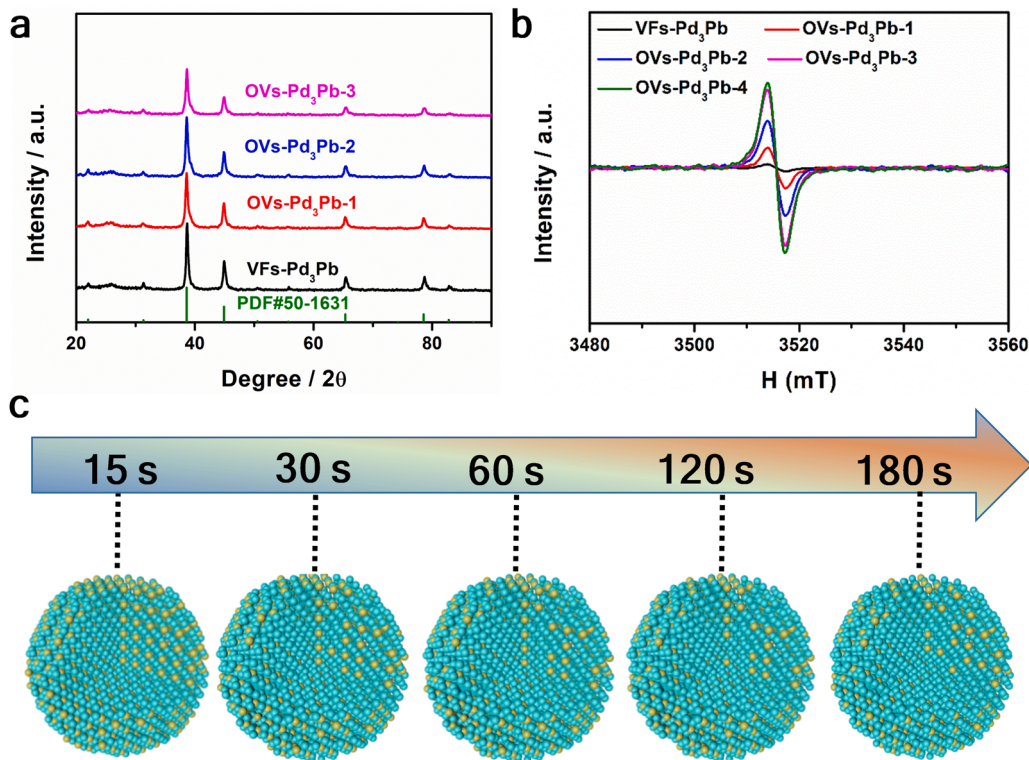


Fig. 2. (a) XRD patterns of the intermetallic VFs-Pd₃Pb and the intermetallic OVs-Pd₃Pb-x (x = 1, 2, 3). (b) Electron spin resonance (ESR) spectroscopy of the intermetallic VFs-Pd₃Pb and the intermetallic OVs-Pd₃Pb-x (x = 1, 2, 3, 4). (c) Synthetic model of OVs-Pd₃Pb-x (x = 1, 2, 3, 4).

the crystalline phase and crystal structure of the intermetallic Pd_3Pb were not destroyed at microwave times of 15 s, 30 s, 60 s, 120 s and 180 s. From Fig. 2b, we can see that the existence of OVs was identified via electron spin resonance (ESR) spectroscopy in the catalysts. Compared with the intermetallic VFs- Pd_3Pb (Fig. S10), which displayed almost no ESR peaks, the other four samples modified showed significant ESR signals, indicating that the order of the intermetallic Pd_3Pb surface was increased and electrons were attracted on the OVs. It can be observed that the ESR signals are strongest when the microwave time is 120 s (OVs- Pd_3Pb -3), indicating that the vacancies degree is highest at this time. From Table S3, we can further know that the level of vacancies did not change significantly when the time was continued to increase to 180 s (OVs- Pd_3Pb -4). Fig. 2c shows a schematic of the vacancies evolution of the intermetallic OVs- Pd_3Pb -X ($X = 1, 2, 3, 4$) catalysts as a function of various microwave time. With the increase of microwave time, the yellow sphere (representing Pb elements) decreases gradually, indicating that Pb vacancies keeps getting larger and finally tends to be stable. In addition, the chemical valence states of Pd and Pb in the intermetallic OVs- Pd_3Pb -X ($X = 1, 2, 3$) and intermetallic VFs- Pd_3Pb catalysts were further researched by X-ray photoelectron spectroscopy (XPS). The total XPS spectra of intermetallic OVs- Pd_3Pb -2 (Fig. S8b) showed the existence of Pd and Pb [30]. It is clear depicted from Fig. S11a that the Pd 3d spectrum of intermetallic VFs- Pd_3Pb shows two main peaks at 335.4 eV and 340.7 eV, which can belong to $\text{Pd 3d}_{5/2}$ and $\text{Pd 3d}_{3/2}$ [32]. The peak intensity gradually increases with enhancing the microwave time, indicating that more Pd is explored to the intermetallic Pd_3Pb surface. And the position of Pd 3d is shifted to the right, which attests to the electron transfer during the microwave process. Moreover, the Pb 4f peak in Fig. S11b exhibits corresponding weakening of the peak intensity and the peak position shift to the left. The peak intensity is weakest when the microwave time is 120 s, further indicating the greatest level of vacancies, which is consistent with the ESR results.

3.2. Synthesis and characterization of pervasive materials

To verify the generality of this favorable synthesis strategy, we further expanded the synthesis to generate intermetallic OVs- Pd_2Sn and intermetallic OVs- Pd_3In by replacing the corresponding precursors in microwave synthesis. First, the successfully prepared intermetallic OVs- Pd_2Sn and intermetallic OVs- Pd_3In comparison samples were demonstrated by a series of physical characterizations such as SEM, TEM, XRD and XPS. As revealed in Fig. S12a-c and Fig. S13, SEM, TEM and TEM-EDX images show that the small size (7.1 nm) of particles with the vacancies are uniformly grown on the CNT and the lattice spacing of OVs- Pd_2Sn is 0.234 nm, which belongs to the (210) face of the intermetallic Pd_2Sn phase. Furthermore, XRD pattern of the intermetallic OVs- Pd_2Sn catalyst matched well with the intermetallic Pd_2Sn (PDF# 52-1515), as shown in Fig. S12d. In addition, the XPS spectrum in Fig. S14 further indicate that Pd and Sn are mostly in the metallic state. Similarly, for the intermetallic OVs- Pd_3In , it is apparently demonstrated that the particles with the vacancies are uniformly grown on the CNT and the average size of about 6.9 nm, as shown in Fig. S15a-c. Moreover, XRD pattern of the OVs- Pd_3In catalyst matched well with the intermetallic Pd_3In reference, as shown in Fig. S15d [46]. The TEM-EDX element mapping images (Fig. S16) demonstrate that Pd and In elements are uniformly scattered in the nanoparticles. In addition, the XPS spectrum in Fig. S17 further indicate that Pd and In are mostly in the metallic state. All this evidence demonstrates the versatility of microwave synthesis of the intermetallic Pd-M ($M = \text{Pb, Sn and In}$) with vacancies catalysts.

3.3. Electrocatalytic properties measurement for NRR

As a green and sustainable route for NH_3 synthesis, electrocatalytic NRR is suitable for distributed and small batch production of NH_3 , which avoids secondary energy consumption in transportation and storage [47]. However, its low reactivity and low selectivity limit its wide application. Therefore, the controllable synthesis of NRR electrocatalysts with high activity, high selectivity and high stability is of great

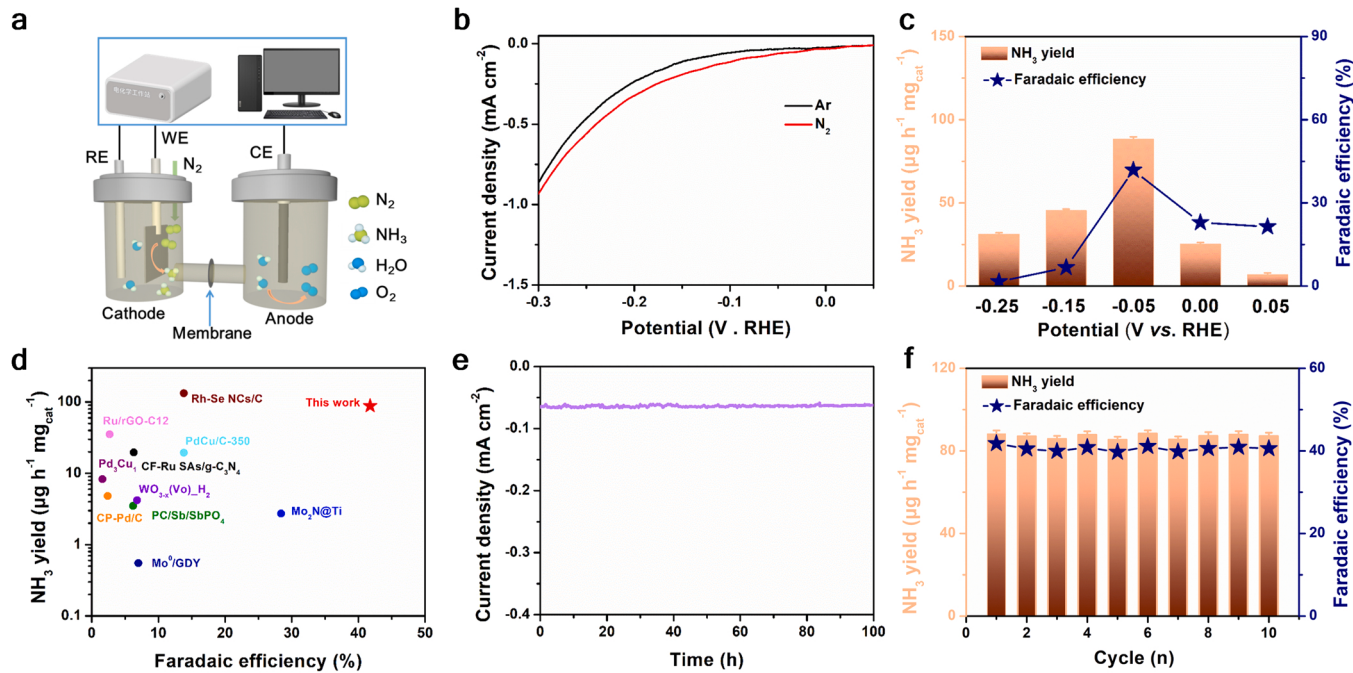


Fig. 3. (a) Schematic diagram of the intermetallic OVs- Pd_3Pb -2 for NH_3 production. (b) Linear sweep voltammetric (LSV) curves of the intermetallic OVs- Pd_3Pb -2 catalyst, the inset is the yield of the intermetallic OVs- Pd_3Pb -2 catalyst. (c) Faradaic efficiencies (FEs) and corresponding NH_3 yield of the intermetallic OVs- Pd_3Pb -2 catalyst at various potential in N_2 -saturated 0.1 M Li_2SO_4 electrolytes. (d) FEs data and corresponding NH_3 production of the intermetallic OVs- Pd_3Pb -2 comparison with different reported catalysts for NRR. (e, f) Long-time chronoamperometry curve and recycling measurement of the intermetallic OVs- Pd_3Pb -2 at -0.05 V vs. RHE.

significance. As shown in Fig. 3a, electrochemical measurements were performed under ambient conditions using an electrocatalytic system in which Nafion membrane divides the two sections of the cell. As can be seen in Fig. 3b, the linear scanning voltammetry (LSV) curves of the intermetallic OVs-Pd₃Pb-2 in N₂-saturated electrolyte show significantly higher current density than in Ar-saturated solution, indicating the possible process of NRR has happened in N₂-saturated electrolyte. The calibration curves of a series of NH₃ and N₂H₄ related standards were detected by indophenol blue method, ion chromatography (IC) and ¹H-nuclear magnetic resonance (¹H NMR) before the experimental tests (Fig. S18–21). As shown in Fig. S22a, the catalyst obtained at –0.05 V vs. RHE has the highest peak at 655 nm, which corresponding the NH₃ yield is the highest. Besides the time-dependent current densities (i-t) at different potentials (0.05 V vs. RHE to –0.25 V vs. RHE) were tested for 3600 s (Fig. S22b), and all performances were stable with ignorable fade. In order to gain reliable Faraday efficiency (FE) and corresponding NH₃ production, three parallel experiments were conducted and the calculated histogram results of mass activity (MA) production and specific activity (SA) production are presented in Fig. 3c and Fig. S23a, respectively. As a result, the intermetallic OVs-Pd₃Pb-2 catalyst indicates an outstanding NRR performance and selectivity in Li₂SO₄ solution. What's more, the FE of H₂ is listed in Fig. S23b, from which we can see distinctly that intermetallic OVs-Pd₃Pb-2 demonstrates the most favourable NRR selectivity at –0.05 V vs. RHE. Under the condition of –0.05 V vs. RHE, the NH₃ yield of intermetallic OVs-Pd₃Pb-2 is 88.3 µg h^{–1} mg_{cat}^{–1} (5.3 µg h^{–1} cm^{–2}), which are 7.7 times and 13.6 times that of Pd₃Pb/CNT (11.4 µg h^{–1} mg_{cat}^{–1} (0.68 µg h^{–1} cm^{–2})) and Pd/CNT (6.5 µg h^{–1} mg_{cat}^{–1} (0.39 µg h^{–1} cm^{–2})), moreover corresponding FE is 41.1% (Fig. 3d and Fig. S24–25). It is the most effective catalyst reported so far in the NRR process at –0.05 V vs. RHE (Table S1). Meanwhile, the by-product N₂H₄ was not tested by the Watt and Chrissp method, which showing the superior selectivity of the intermetallic OVs-Pd₃Pb-2 catalyst (Fig. S26). In addition, NH₃ yields were measured by IC and ¹H NMR with values similar to those of UV-vis spectra (Fig. S27–29). The UV-vis spectrophotometric results for N-(1-naphthyl)-ethylenediamine hydrochloride shows no N source in the detection environment (Fig. S30–31). As shown in Fig. S32, no significant NH₃ peak appeared during the detection.

Furthermore, a series of experiments were performed to investigate the NRR performance of intermetallic VFs-Pd₃Pb and intermetallic OVs-Pd₃Pb-X (X = 1, 2, 3) with different defect levels. Fig. S33a shows the LSV curves of intermetallic VFs-Pd₃Pb and intermetallic OVs-Pd₃Pb-X (X = 1, 2, 3) in N₂-saturated 0.1 M Li₂SO₄ solution. Fig. S33b displays the i-t curves of intermetallic VFs-Pd₃Pb and intermetallic OVs-Pd₃Pb-X (X = 1, 2, 3) in N₂-saturated at –0.05 V vs. RHE. The UV-vis spectra of NH₃ after electrocatalysis was presented in Fig. S33c. Notably, the highest NH₃ yield was obtained via OVs-Pd₃Pb-2 compared with the other three NRR electrocatalysts. At a low overpotential of –0.05 V vs. RHE, its NH₃ yield and FE reached 88.3 µg h^{–1} mg_{cat}^{–1} and 41.1%, respectively (Fig. S33d), significantly higher than that of VFs-Pd₃Pb (7.2 µg h^{–1} mg_{cat}^{–1} and 8.4%). As can be seen from Fig. S34, the TOF of the OVs-Pd₃Pb-2 catalyst at –0.05 V vs. RHE achieves 27.3 h^{–1}, which is preferred to the VFs-Pd₃Pb (2.2 h^{–1}), indicating that OVs-Pd₃Pb-2 catalyst has a favorable intrinsic activity. To assess the electrochemically active specific surface area, we tested the electrochemical double layer capacitance (C_{dl}) of intermetallic VFs-Pd₃Pb and intermetallic OVs-Pd₃Pb-X (X = 1, 2, 3) (Fig. S35–36). The results show that the C_{dl} of intermetallic OVs-Pd₃Pb-2 is 1.53 mF cm^{–2}, which is significantly better than the other catalysts. As is shown in Fig. S37, we can see that the NH₃ yield of the intermetallic OVs-Pd₃Pb-2, OVs-Pd₂Sn and OVs-Pd₃In are better than Pd/CNT catalyst. This strategy is also considered to show great potential for the production of many other Pd-based intermetallic compound with defects. In addition, to our knowledge, ordered atomic arrangements with defects are scarcely reported, which are expected to exhibit excellent catalytic properties.

What's more, the stability of catalyst is another key indicator of

catalyst performance for NRR reaction. It is obviously demonstrated from Fig. 3e that the OVs-Pd₃Pb-2 catalyst shows almost no decaying trend in current density and good NH₃ yield after 100 h of electrolysis at –0.05 V vs. RHE, which indicates that the intermetallic OVs-Pd₃Pb-2 catalyst has good electrochemical NRR stability (Fig. S38). Besides, it can be seen from Fig. S39 that the NH₃ yield under other conditions is negligible compared with the N₂-saturated environment. To demonstrate the importance of introducing N₂ in the reaction process (Fig. S40a), we performed an electrochemical NRR test at –0.05 V vs. RHE under alternating N₂-saturated and Ar-saturated electrolytes. It is obvious that NH₃ can be produced in large quantities in N₂-saturated Li₂SO₄ solutions but hardly found in Ar-saturated solutions. In addition, it can be seen from Fig. S40b that the NH₃ yield of the intermetallic OVs-Pd₃Pb-2 catalyst shows a linear positive trend with increasing the electrocatalysis NRR time. Most importantly, the results of the cycling experiments (Fig. 3f and Fig. S41) clearly show that the intermetallic OVs-Pd₃Pb-2 catalyst without a significant decrease in NH₃ yield and FE after the tenth consecutive cycle. Otherwise, it is apparent from the SEM (Fig. S42a) and TEM images (Fig. S42b) that the intermetallic OVs-Pd₃Pb-2 catalyst retain the initial structure after stability testing. XRD (Fig. S43a) and XPS (Fig. S43b–c) results show no significant change in the peak position and intensity compared to the original data, further demonstrating the better stability of the catalyst.

3.4. In situ Raman, in situ ATR-SEIRAS and DFT technique for NRR

In situ Raman spectroscopy, in situ ATR-SEIRAS and DFT technique were used to explore the specific mechanisms of OVs and the ordered atomic arrangement in the NRR process. A Raman peak of the stretching vibration at about 1000 cm^{–1} in the dotted box assigned to the sulfate radical species absorbed on the surface of catalysts, suggesting the excellent wettability for the electrolyte. For the Pd₃Pb with the optimal OVs (Fig. 4a), the peak NH₃ stretching vibration at about 1644 cm^{–1} will appear soon [48], indicating that the OVs-induced the intermetallic Pd₃Pb occurs in the NRR process, suggesting the occurrence of N₂ chemisorption and activation on OVs-induced unsaturated Pb sites of the intermetallic Pd₃Pb in the NRR process. In contrast, no or weak NH₃ stretching peak can be observed on OVs-free intermetallic Pd₃Pb and Pd₃Pb/CNT (Fig. S44) with the extension of the reaction time, demonstrating their poor N₂ activation. As can be seen from Fig. S45, the Bader charge change (Δq) for intermetallic VFs-Pd₃Pb without vacancies is 0.871 e, and the Δq for the intermetallic OVs-Pd₃Pb-2 catalyst is 0.952 e, indicating that the presence of OVs facilitate electron transfer and thus boost the NRR process. The density of total states (DOS) curve is used to illustrate the variation of electrons around the Fermi energy level (E = 0 eV). Specifically, the fundamental charge density at the Fermi energy level for the VFs-Pd₃Pb catalyst without vacancies in Fig. 4b is far away 0 eV. In the intermetallic OVs-Pd₃Pb-2 with vacancies, which leads to an increase in the charge density (Fig. 4c). On the one hand, the vacancies mainly occur in the conduction band, and it can be seen that the new peak of Pd caused by the vacancies appear in the conduction band. On the other hand, after the vacancies occur, the energy level changes into a continuous state, which are conducive to the electron conduction of the system. From Fig. 4d, the whole path diagram of electrocatalytic NRR can be clearly shown. Moreover, the N₂ adsorption capacity of intermetallic VFs-Pd₃Pb and intermetallic OVs-Pd₃Pb-2 was investigated using the N₂ programmed ramp-up desorption (N₂-TPD) method. As shown in Fig. S46, the high signal of chemisorption of the ordered atomic arrangement with intermetallic OVs-Pd₃Pb-2 indicates that the adsorption of N₂ is higher than that of intermetallic VFs-Pd₃Pb [49]. Otherwise, it can be known from Fig. 4e that the energy barriers for the conversion of N₂ to NNH^{*} (the rate-determining step, Table S4), and it can be seen that the energy barrier decreases substantially after the inclusion of the ordered atomic arrangement and vacancies, which facilitates the reaction (Fig. S47–50). The proton supply was further tested using the in situ ATR-SEIRAS technique, and the data are shown in

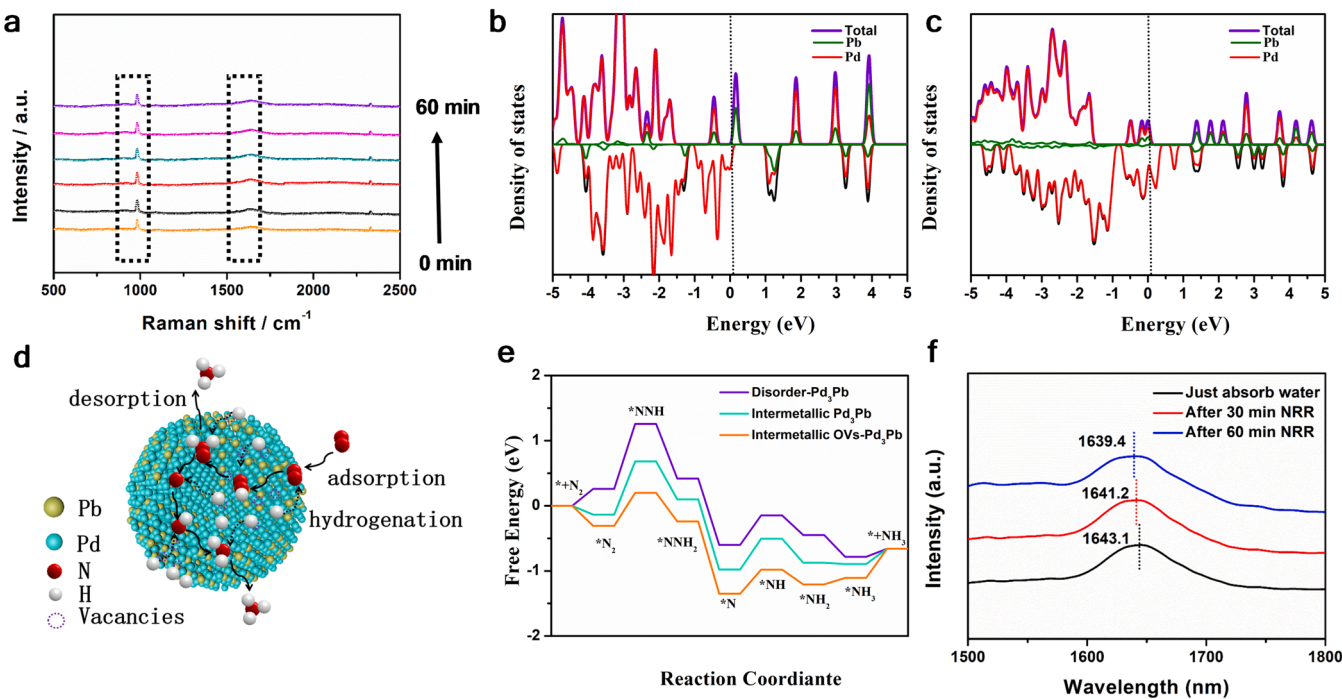


Fig. 4. (a) Time-resolved *in situ* Raman spectra of the intermetallic OVs-Pd₃Pb-2 during the NRR electrolysis at -0.05 V vs. RHE under N₂ atmosphere for 1 h. (b, c) The density of states (DOS) for the intermetallic VFs-Pd₃Pb and the intermetallic OVs-Pd₃Pb-2. (d) Simplistic mechanism of N₂ production on the surface of OVs-Pd₃Pb-2. (e) The free energy profile of NRR pathway on the disorder Pd₃Pb, intermetallic VFs-Pd₃Pb and the intermetallic OVs-Pd₃Pb-2. (f) In situ attenuated total reflectance surface-enhanced infrared absorption spectroscopy (ATR-SEIRAS) spectrum of H-OH for NRR process in the intermetallic OVs-Pd₃Pb-2 with various times.

Fig. 4f. The electrocatalyst was immersed in 0.1 M Li₂SO₄ solution before the electrochemical reaction, and a bending vibration peak of H-OH bond appeared at 1643.1 cm⁻¹ [50]. As the reaction proceeds, the peak shows a clear red shift trend from 1643.1 cm⁻¹ to 1639.4 cm⁻¹, indicating that the H-OH bond becomes weaker with the continuation of NRR. Finally, *in situ* Raman spectroscopy, *in situ* ATR-SEIRAS and DFT technique further demonstrate the synergy mechanism that the ordered atomic arrangement drives nitrogen adsorption and promotes water cleavage to supply protons, while OVs on Pd₃Pb-2 can further stabilize the *N₂/*N₂H to break the proportionality while destabilizing *NH₂/*NH₃ and regulate lowers the energy barrier for the conversion of N₂ to NNH* (the rate-determining step), resulting in good NRR activity at low overpotential.

4. Conclusions

In short, the small size (< 10 nm) of intermetallic PdM (M = Pb, Sn, In) with ordered vacancies (OVs) are successfully prepared by ultrafast and solvent-free microwave method for the first time. The microwave method is simple, rapid (60 s) and high production (82.0%), and the degree of defects can be adjusted by changing the microwave time. The synthesis of intermetallic compound catalysts can obtain gram-level products. Under the condition of -0.05 V vs. RHE, the NH₃ yield of intermetallic OVs-Pd₃Pb-2 is 88.3 μ g h⁻¹ mg_{cat}⁻¹, which is 13.6 times that of Pd/CNT (6.5 μ g h⁻¹ mg_{cat}⁻¹), otherwise corresponds to FE is 41.1%. TOF of the OVs-Pd₃Pb-2 catalyst at -0.05 V vs. RHE achieves 27.3 h⁻¹, which is preferred to the VFs-Pd₃Pb (2.2 h⁻¹), indicating that OVs-Pd₃Pb-2 catalyst has a favorable intrinsic activity. It is the most effective catalyst reported so far in the nitrogen reduction process at -0.05 V vs. RHE. *In situ* Raman spectroscopy, *in situ* ATR-SEIRAS and DFT technique further display the synergy mechanism that the ordered atomic arrangement drives nitrogen adsorption and promotes water cleavage to supply protons, while OVs on Pd₃Pb-2 can further stabilize the *N₂/*N₂H to break the proportionality while destabilizing *NH₂/*NH₃ and regulate lowers the energy barrier for the conversion of N₂ to NNH* (the

rate-determining step), resulting in good NRR activity at low overpotential. Therefore, this work not only engineering ordered vacancies and atomic arrangement over the intermetallic nanocatalysts for synergistically promoting electrocatalytic performance for the first time, but also providing a method to stabilize the vacancy by forming ordered structure.

CRediT authorship contribution statement

Zuochao Wang: Investigation, Data curation, Conceptualization, Formal analysis, Validation, Writing – original draft. **Jiao Liu:** Investigation, Data curation, Conceptualization, Formal analysis, Validation, Writing – original draft. **Xueke Wu:** Data curation, Conceptualization. **Nanzhu Nie:** Formal analysis. **Dan Zhang:** Validation. **Hongdong Li:** Validation. **Huan Zhao:** Formal analysis. **Jianping Lai:** Conceptualization, Writing – review & editing, Supervision, Funding acquisition. **Lei Wang:** Writing – review & editing, Funding acquisition, Supervision.

Declaration of Competing Interest

The authors declare that they have no known competing financial interests or personal relationships that could have appeared to influence the work reported in this paper.

Acknowledgment

This work was supported by the National Natural Science Foundation of China (51772162, 22001143, and 52072197), Youth Innovation and Technology Foundation of Shandong Higher Education Institutions, China (2019KJC004), Outstanding Youth Foundation of Shandong Province, China (ZR2019JQ14), Taishan Scholar Young Talent Program (tsqn201909114, tsqn201909123), Natural Science Foundation of Shandong Province (ZR2020YQ34), Major Scientific and Technological Innovation Project (2019JZZY020405), and Major Basic Research Program of Natural Science Foundation of Shandong Province under Grant

(ZR2020ZD09).

Appendix A. Supporting information

Supplementary data associated with this article can be found in the online version at [doi:10.1016/j.apcatb.2022.121465](https://doi.org/10.1016/j.apcatb.2022.121465).

References

- [1] S. Andersen, V. Čolić, S. Yang, J. Schwalbe, A. Nielander, J. McEnaney, K. Enemark, J. Baker, A. Singh, B. Rohr, M. Statt, S. Blair, S. Mezzavilla, J. Kibsgaard, P. Vesborg, M. Cargnello, S. Bent, T. Jaramillo, I. Stephens, J. Nørskov, I. Chorkendorff, *Nature* 570 (2019) 504–508, <https://doi.org/10.1038/s41586-019-1260-x>.
- [2] B.H.R. Suryanto, K. Matuszek, J. Choi, R.Y. Hodgetts, H.L. Du, J.M. Bakker, C.S. M. Kang, P.V. Cherepanov, A.N. Simonov, D.R. MacFarlane, *Science* 372 (2021) 1187–1191, <https://doi.org/10.1126/science.abg2371>.
- [3] Z.W. Seh, J. Kibsgaard, C.F. Dickens, I. Chorkendorff, J.K. Nørskov, T.F. Jaramillo, *Science* 355 (2017) 146–157, <https://doi.org/10.1126/science.aad4998>.
- [4] Y. Ashida, K. Arashiba, K. Nakajima, Y. Nishibayashi, *Nature* 568 (2019) 536–540, <https://doi.org/10.1038/s41586-019-1134-2>.
- [5] J. Chen, R. Crooks, L. Seefeldt, K. Bren, R. Bullock, M. Darenbourg, P. Holland, B. Hoffman, M. Janik, A. Jones, M. Kanatzidis, P. King, K. Lancaster, S. Lyman, P. Pfromm, W. Schneider, R. Schrock, *Science* 360 (2018) 873, <https://doi.org/10.1126/science.aar6611>.
- [6] W. Kang, C.C. Lee, A.J. Jasniewski, M.W. Ribbe, Y. Hu, *Science* 368 (2020) 1381–1385, <https://doi.org/10.1126/science.aae6748>.
- [7] M. Wang, S. Liu, T. Qian, J. Liu, J. Zhou, H. Ji, J. Xiong, J. Zhong, C. Yan, *Nat. Commun.* 10 (2019) 341, <https://doi.org/10.1038/s41467-018-08120-x>.
- [8] Y. Song, D. Johnson, R. Peng, D.K. Hensley, P.V. Bonnesen, L. Liang, J. Huang, F. Yang, F. Zhang, R. Qiao, A.P. Baddorf, T.J. Tschaplinski, N.L. Engle, M. C. Hatzell, Z. Wu, D.A. Cullen, H.M. Meyer, B.G. Sumpter, A.J. Rondinone, *Sci. Adv.* 4 (2018), e1700336, <https://doi.org/10.1126/sciadv.1700336>.
- [9] H.K. Lee, C.S.L. Koh, Y.H. Lee, C. Liu, I.Y. Phang, X. Han, C.K. Tsung, X.Y. Ling, 4, *Sci. Adv.* (2018) eaar3208, <https://doi.org/10.1126/sciadv.aar3208>.
- [10] M. Arif, G. Yasin, L. Luo, W. Ye, M.A. Mushtaq, X. Fang, X. Xiang, S. Ji, D. Yan, *Appl. Catal. B Environ.* 265 (2019), 118559, <https://doi.org/10.1016/j.apcatb.2019.118559>.
- [11] X.F. Li, Q.K. Li, J. Cheng, L. Liu, Q. Yan, Y. Wu, X.-H. Zhang, Z.-Y. Wang, Q. Qiu, Y. Luo, *J. Am. Chem. Soc.* 138 (2016) 8706–8709, <https://doi.org/10.1021/jacs.6b04778>.
- [12] C. Ling, Y. Zhang, Q. Li, X. Bai, L. Shi, J. Wang, *J. Am. Chem. Soc.* 141 (2019) 18264–18270, <https://doi.org/10.1021/jacs.9b09232>.
- [13] L. Han, X. Liu, J. Chen, R. Lin, H. Liu, F. Lu, S. Bak, Z. Liang, S. Zhao, E. Stavitski, J. Luo, R. Adzic, H. Xin, *Angew. Chem. Int. Ed.* 131 (2018) 2343–2347, <https://doi.org/10.1002/anie.201811728>.
- [14] L.-F. Gao, Y. Cao, C. Wang, X.-W. Yu, W.-B. Li, Y. Zhou, B. Wang, Y. Yao, C.-P. Wu, W.-J. Luo, Z.-G. Zou, *Angew. Chem. Int. Ed.* 60 (2021) 5257–5261, <https://doi.org/10.1002/anie.202015496>.
- [15] G. Ozin, H. Wang, L. Wang, Q. Wang, S. Ye, W. Sun, Y. Shao, Z. Jiang, Q. Qiao, Y. Zhu, P. Song, D. Li, L. He, X. Zhang, J. Yuan, T. Wu, *Angew. Chem. Int. Ed.* 57 (2018) 12360–12364, <https://doi.org/10.1002/anie.201805514>.
- [16] Q. Qin, Y. Zhao, M. Schmallegger, T. Heil, J. Schmidt, R. Walczak, G. Gescheidt, H. Jiao, M. Oschatz, *Angew. Chem. Int. Ed.* 58 (2019) 13101–13106, <https://doi.org/10.1002/anie.201906056>.
- [17] H. Su, L. Chen, Y. Chen, Y. Wu, X. Wu, R. Si, W. Zhang, Z. Geng, J. Zeng, *Angew. Chem. Int. Ed.* 59 (2020) 20411–20416, <https://doi.org/10.1002/anie.202009217>.
- [18] C. Guo, X. Liu, L. Gao, X. Kuang, X. Ren, X. Ma, M. Zhao, H. Yang, X. Sun, Q. Wei, *Appl. Catal. B Environ.* 263 (2019), 118296, <https://doi.org/10.1016/j.apcatb.2019.118296>.
- [19] L. Sun, Y. Zhao, F. Li, W. Li, Y. Li, C. Liu, Z. Zhao, Y. Shan, Y. Ji, *Angew. Chem. Int. Ed.* 60 (2021) 20331–20341, <https://doi.org/10.1002/anie.202104918>.
- [20] X. Wang, J. Yang, M. Salla, S. Xi, Y. Yang, M. Li, F. Zhang, M. Zhu, S. Huang, S. Huang, Y. Zhang, Q. Wang, *Angew. Chem. Int. Ed.* 60 (2021) 18721–18727, <https://doi.org/10.1002/anie.202105536>.
- [21] F. Zhou, L. Azofra, M. Alagéle, M. Kar, A. Simonov, C. James, C. Sun, X. Zhang, D. Mac, *Energy Environ. Sci.* 10 (2017) 2516–2520, <https://doi.org/10.1039/C7EE02716H>.
- [22] J. McEnaney, A. Singh, J. Schwalbe, J. Kibsgaard, J. Lin, M. Cargnello, T. Jaramillo, J. Nørskov, *Energy Environ. Sci.* 10 (2017) 1621–1630, <https://doi.org/10.1039/C7EE01126A>.
- [23] C. Tang, S.Z. Qiao, *Chem. Soc. Rev.* 48 (2019) 3166–3180, <https://doi.org/10.1039/c9cs00280d>.
- [24] J. Wang, L. Yu, L. Hu, G. Chen, H. Xin, X. Feng, *Nat. Commun.* 9 (2018) 1795, <https://doi.org/10.1038/s41467-018-04213-9>.
- [25] D. Bao, Q. Zhang, F. Meng, H. Zhong, M. Shi, Y. Zhang, J. Yan, Q. Jiang, X. Zhang, *Adv. Mater.* 29 (2017), 1604799, <https://doi.org/10.1002/adma.201604799>.
- [26] H. Jin, L. Li, X. Liu, C. Tang, W. Xu, S. Chen, L. Song, Y. Zheng, S. Qiao, *Adv. Mater.* 31 (2019), 1902709, <https://doi.org/10.1002/adma.201902709>.
- [27] Y. Wen, Z. Zhuang, H. Zhu, J. Hao, K. Chu, F. Lai, W. Zong, C. Wang, P. Ma, W. Dong, S. Lu, T. Liu, M. Du, *Adv. Energy Mater.* 11 (2021), 2102138, <https://doi.org/10.1002/aenm.202102138>.
- [28] J.T. Ren, C.Y. Wan, T.Y. Pei, X.W. Lv, Z.Y. Yuan, *Appl. Catal. B Environ.* 266 (2020), 118633, <https://doi.org/10.1016/j.apcatb.2020.118633>.
- [29] X. Wang, M. Luo, J. Lan, M. Peng, Y. Tan, *Adv. Mater.* 33 (2021), 2007733, <https://doi.org/10.1002/adma.202007733>.
- [30] J. Guo, L. Gao, X. Tan, Y. Yuan, J. Kim, Y. Wang, H. Wang, Y.J. Zeng, S.I. Choi, S. C. Smith, H. Huang, *Angew. Chem. Int. Ed.* 60 (2021) 10942–10949, <https://doi.org/10.1002/anie.202100307>.
- [31] M. Chen, Y. Yan, M. Gebre, C. Ordóñez, F. Liu, L. Qi, A. Lamkins, D. Jing, K. Dolge, B. Zhang, P. Heintz, D.P. Shoemaker, B. Wang, W. Huang, *Angew. Chem. Int. Ed.* 60 (2021) 18309–18317, <https://doi.org/10.1002/anie.202106515>.
- [32] J. Guo, H. Wang, F. Xue, D. Yu, L. Zhang, S. Jiao, Y. Liu, Y. Lu, M. Liu, S. Ruan, Y. J. Zeng, C. Ma, H. Huang, *J. Mater. Chem. A* 7 (2019) 20247–20253, <https://doi.org/10.1039/c9ta07519d>.
- [33] Y. Tong, H. Guo, D. Liu, X. Yan, P. Su, J. Liang, S. Zhou, J. Liu, G.Q. Lu, S.X. Dou, *Angew. Chem. Int. Ed.* 59 (2020) 7356–7361, <https://doi.org/10.1002/anie.202002029>.
- [34] B. Huang, Y.F. Wu, B.B. Chen, Y. Qian, N.G. Zhou, N. Li, Chin. J. Catal. 42 (2021) 1160–1167, [https://doi.org/10.1016/S1872-2067\(20\)63745-7](https://doi.org/10.1016/S1872-2067(20)63745-7).
- [35] K. Chu, Q.Q. Li, Y.P. Liu, J. Wang, Y.H. Cheng, *Appl. Catal. B Environ.* 267 (2020) 8, <https://doi.org/10.1016/j.apcatb.2020.118693>.
- [36] A.L. Wang, L. Zhu, Q. Yun, S. Han, L. Zeng, W. Cao, X. Meng, J. Xia, Q. Lu, *Small* 16 (2020) 2003782, <https://doi.org/10.1002/smll.202003782>.
- [37] C.L. Yang, P. Yin, J.Y. Liu, M.X. Chen, Q.O. Yan, Z.S. Wang, S.L. Xu, S.Q. Chu, C. H. Cui, H.X. Ju, J.F. Zhu, Y. Lin, J.L. Shui, H.W. Liang, *Science* 374 (2021) 459–464, <https://doi.org/10.1126/science.abj9980>.
- [38] Z. Cui, H. Chen, M. Zhao, D. Marshall, Y. Yu, H. Abruna, F.J. DiSalvo, *J. Am. Chem. Soc.* 136 (2014) 10206–10209, <https://doi.org/10.1021/ja504573a>.
- [39] T.Y. Yoo, J.M. Yoo, A.K. Sinha, M.S. Bootharaju, E. Jung, H.S. Lee, B.H. Lee, J. Kim, W.H. Antink, Y.M. Kim, J. Lee, E. Lee, D.W. Lee, S.P. Cho, S.J. Yoo, Y.E. Sung, T. Hyeon, *J. Am. Chem. Soc.* 142 (2020) 14190–14200, <https://doi.org/10.1021/jacs.0c05140>.
- [40] T. Shen, S. Chen, R. Zeng, M. Gong, T. Zhao, Y. Lu, X. Liu, D. Xiao, Y. Yang, J. Hu, D. Wang, H.L. Xin, H.D. Abruna, *ACS Catal.* 10 (2020) 9977–9985, <https://doi.org/10.1021/acscatal.0c01537>.
- [41] J. Su, H. Zhao, W. Fu, W. Tian, X. Yang, H. Zhang, F. Ling, Y. Wang, *Appl. Catal. B Environ.* 265 (2020), 118589, <https://doi.org/10.1016/j.apcatb.2020.118589>.
- [42] M. Kim, B. Lee, H. Ju, S.W. Lee, J. Kim, *Adv. Mater.* 31 (2019) 1901977, <https://doi.org/10.1002/adma.201901977>.
- [43] L. Shao, W. Zhang, M. Armbruster, D. Teschner, F. Girsdsies, B. Zhang, O. Timpe, M. Friedrich, R. Schlogl, D.S. Su, *Angew. Chem. Int. Ed.* 50 (2011) 10231–10235, <https://doi.org/10.1002/anie.201008013>.
- [44] R. Kadiyath, G.V. Ramesh, E. Koudelkova, T. Tanabe, M. Ito, M. Manikandan, S. Ueda, T. Fujita, N. Umezawa, H. Noguchi, K. Ariga, H. Abe, *Energy Environ. Sci.* 8 (2015) 1685–1689, <https://doi.org/10.1039/c4ee03746d>.
- [45] Q. Feng, S. Zhao, D. He, S. Tian, L. Gu, X. Wen, C. Chen, Q. Peng, D. Wang, Y. Li, *J. Am. Chem. Soc.* 140 (2018) 2773–2776, <https://doi.org/10.1021/jacs.7b13612>.
- [46] Q. Feng, S. Zhao, Y. Wang, J. Dong, W. Chen, D. He, W. Wang, J. Yang, Y. Zhu, H. Zhu, L. Gu, Z. Li, Y. Liu, R. Yu, J. Li, Y. Li, *J. Am. Chem. Soc.* 139 (2017) 7294–7301, <https://doi.org/10.1021/jacs.7b01471>.
- [47] Z. Sun, R. Huo, C. Choi, S. Hong, T. Wu, J. Qiu, C. Yan, Z. Han, Y. Liu, Y. Soo, Y. Jung, *Nano Energy* 62 (2019) 869–875, <https://doi.org/10.1016/j.nanoen.2019.06.019>.
- [48] F. Cheng, W. Xu, G. Fan, J. Chen, J. Li, L. Zhang, S. Zhu, X. Su, J. Chen, *Angew. Chem. Int. Ed.* 59 (2020) 3511–3516, <https://doi.org/10.1002/anie.201914335>.
- [49] H. Zhao, D. Zhang, H. Li, W. Qi, X. Wu, Y. Han, W. Cai, Z. Wang, J. Lai, L. Wang, *Adv. Energy Mater.* 10 (2020) 2002131, <https://doi.org/10.1002/aenm.202002131>.
- [50] Z. Dong, F. Lin, Y. Yao, L. Jiao, *Adv. Energy Mater.* 9 (2019) 1902703, <https://doi.org/10.1002/aenm.201902703>.